Millimeter-Wave Interferometry for Opaque Particle-Laden Flows

Nicolas Rasmont, *Graduate Student Member, IEEE*, Hussein Al-Rashdan, Gregory Elliott, Joshua Rovey, and Laura Villafañe

Abstract— A novel method to measure the concentration of particles in optically opaque particle-laden flows is presented. This method is based on the principle of millimeter wave interferometry, using a fully-integrated frequency modulated continuous-wave (FMCW) radar operating between 77 and 81 GHz to measure path-integrated particle concentrations between the radar and a reflector. The instrument is capable of quantitative, high-speed (20 kHz) path-integrated concentration measurements in dispersed multiphase flows with concentrations one to two orders of magnitude higher than those at reach with state-of-the-art optical methods. The interferometer was demonstrated and calibrated for path-integrated number concentrations up to $(4.36 \pm 0.24) \times 10^8$ m^{-2} using glass microspheres with a mean diameter of 109.2 μm. Two independent measurements of particle size distribution (PSD) were performed using X-ray microtomography and dry sieving. The calibration setup relied on high-resolution particle shadowgraphy applied to individual thin particle streams and used multistreams superposition to reproduce large optical depths in a controlled particle-air mixture. The instrument exhibited excellent linearity and low error during the calibration, with a phase shift-to-number concentration slope of $(1.378 \pm 0.043) \times 10^{-7}$ m^2, validating the measurement concept and paving the way for practical applications. The leading uncertainties are discussed, providing guidelines for exploiting the measurement concept without necessarily performing a direct calibration.

Index Terms— Interferometry, millimeter-wave (mm-Wave), multiphase flow, permittivity, radar.

I. INTRODUCTION

PARTICLE-LADEN flows, also known as dispersed multiphase flows, are defined by the presence of small discrete particles (bubbles, droplets, or grains) suspended in a continuous fluid [1]. They are important to a wide range of natural and man-made environments, including, among others, fluidized bed reactors [2], [3] and sediment transport [4], [5]. Particle-laden flows are the direct cause of a number of hazards with significant human and material costs. Dust explosions caused 119 deaths and hundreds of millions of dollars in property damage in the United States between 1980 and 2005 [6]. Aeolian soil erosion is a significant contributor to desertification and loss of arable land [7]. Dispersed multiphase flows are also of high importance during the landing of aerospace vehicles on unprepared surfaces. Dust lifted by the downwash of a rotorcraft can lead to a complete or partial loss of visibility during landing, a dangerous condition called brownout. Spatial disorientation due to brownout has been the cause of 400 rotorcraft losses at a cost of 152 lives and one billion United States Dollar (USD) in damage in the U.S. Army alone between 2002 and 2015 [8]. The interactions between rocket plumes and granular planetary surfaces (plume-surface interactions or PSI) during the landing of a human-class spacecraft on the Moon or Mars give rise to a number of challenges. The erosion of the surface by the jet generates multiple tons of supersonic, highly abrasive ejecta capable of damaging the spacecraft and any infrastructure nearby [9], [10], and lead to the formation of a crater deep enough to topple or bury the lander [11], [12], [13]. The ejecta cloud itself can blind pilots and landing sensors during terminal descent [14].

Improving understanding of particle-laden flows is critical for industrial and aerospace safety, environmental preservation, and a wide range of other fields. Theoretical and numerical descriptions of dispersed multiphase flows are challenged by the coupling between a discrete inertial particle phase and the continuum flow phase, generally turbulent. Despite significant advances in the last 30 years from experiments and simulations, numerical and theoretical models of multiphase flows are still not suitable for predictive capabilities in many realistic applications. Current state-of-the-art point-particle Lagrangian models coupled with an Eulerian flow description can be used to simulate thousands to millions of particles at the expense of computational power [15], [16], [17], but these numbers are still far from practical real-life situations involving billions or trillions of particles [18], [19]. In addition, the fidelity of those simulations depends on the range of particle-fluid nondimensional parameters that dominate the two-way coupled interactions being modeled. The computational cost of Eulerian-Eulerian models on the other hand is more permissive for large simulations but they necessitate constitutive models for interparticle and interphase dynamics [20], [21].

Experimental research in particle-laden flows has been much benefited from the rapid development of high-speed and high-resolution cameras in the last two decades. While essential for dilute conditions, quantitative concentration measurements via imagining are challenged as concentration increases due

to apparent particle overlap and ghost particles [16]. Laser and phase Doppler anemometry (PDA) and laser diffraction techniques are also commonly used to measure particle concentrations, velocities or sizes [22], [23], [24]. They are most suitable for dilute conditions, with measurement uncertainties that increase with concentration. At volume fractions above 0.1%–0.01%, depending on the particle size and material properties, optical diagnostics fail due to the opacity of the particle-fluid mixture [25], [26]. Measurements in particle-laden flows also face other challenges absent in single-phase flows as particles can coat or damage experimental hardware through erosion, impact, mechanical jamming, or triboelectric charging [27], hindering the use of classical intrusive instrumentation.

Some nonintrusive, nonoptical diagnostics are applicable to opaque flows. X-ray transmission computed tomography (CT) [28], X-ray diffraction tomography [29], gamma-ray transmission CT [30], neutron transmission CT [31], and positron emission CT [32], use ionizing radiations to characterize opaque flows with extremely high volume fractions, theoretically up to 100%, at high spatial resolution. However, they suffer from high cost, low temporal resolution, and bring a range of health and safety risks. Other nonionizing methods include nuclear magnetic resonance (NMR) imaging [33], ultrasound tomography [34], microwave tomography [35], and a set of related electrical tomography methods: capacitance tomography (ECT) [36], resistivity tomography (ERT) [37], and impedance tomography (EIT) [38]. They typically suffer from high attenuation, low acquisition frequency, and, with the exception of NMR imaging, have relatively low resolution, on the order of centimeters. Most of those nonoptical diagnostics require the experiment to fit within the instrument, restricting their applicability for fluid-driven experiments.

This work presents a novel method to measure the volume fraction in particle-laden flows that overcomes some of the limitations of existing diagnostics in high concentration environments. Originally developed for studying plume-surface interactions in planetary landing experiments [39], it is amenable to the study of opaque gas-particle mixtures where optical diagnostics fail due to excessive attenuation. The method is based on the principle of millimeter-wave (mm-Wave) interferometry, which has been extensively investigated for medical [40], [41] and industrial [42], [43] purposes. mm-Wave interferometric techniques are also used to measure electron densities in plasma devices [44], [45]. In the current study, a fully integrated, frequency-modulated continuous-wave (FMCW) radar operating between 77 and 81 GHz illuminates the area-under-test, tracking the phase shift of a wave bouncing off a reflector located at a known, fixed position. The FMCW mode of operation allows the instrument to discriminate between the reflector echo and clutter without requiring the complex quasi-optical beam-forming system of continuous-wave interferometers [46]. The phase of the electromagnetic wave provides the concentration of particles integrated along the line of sight between the radar and the reflector at a high repetition rate, independently of the size distribution of the material, and for a range of concentrations at least one order of magnitude higher than optical techniques.

Sampling rates of 20 kHz were achieved in this work, but several MHz are possible using a dedicated, optimized radar system. The sensor compares favorably in terms of cost, power, size, and mass with conventional nonintrusive particle concentration diagnostics and unlike most of them, can be extended to field measurements.

This article is an extension of the works presented in [47] and [48]. Focusing on the specific use case of an ongoing plume-surface interaction experiment, they served to demonstrate the potential of mm-Wave interferometry for rapidly varying optically opaque environments. This manuscript presents a refined version of a mm-Wave interferometer for particle concentrations that is application agnostic. The theoretical foundations of the technique are revisited in detail in Section II. The instrument and the experiment specifically designed for its demonstration and calibration are described in Section III, with their results presented in Section IV. This work also extends on detailed propagation of uncertainties not previously explored, essential to improve the accuracy of the calibrated instrument and to evaluate the validity of the theoretical models. The second objective is achieved using Monte-Carlo (MC) simulations fed with probability distributions for the unknown parameters in the models derived for the Maxwell-Garnett equation. The analysis in Section V suggests that calibration-free measurements are possible and provides a framework to identify which particle properties need to be more accurately known to minimize measurement uncertainties. Published experimental data in particle-laden jets is used to evaluate the potential of the new instrument to extend the range of particle concentrations that can be quantified. The strength and limits of mm-Wave interferometry are also discussed, together with recommendations for future developments.

II. THEORY OF OPERATION

A. Fundamentals

For the purpose of modeling electromagnetic wave propagation, particle-laden flows with randomly distributed particles can be assumed to behave as a homogeneous, isotropic material with an effective dielectric constant ε_{eff}. The Maxwell-Garnett equation shown in (1) [49] provides ε_{eff} as a function of the volume fraction of particles δ (ratio of the volume of particles to total volume), the dielectric constant of the particle material ε_i, and the dielectric constant of the host fluid ε_h

$$\frac{\varepsilon_{\text{eff}} - \varepsilon_h}{\varepsilon_{\text{eff}} + 2\varepsilon_h} = \delta \frac{\varepsilon_i - \varepsilon_h}{\varepsilon_i + 2\varepsilon_h}. \tag{1}$$

The Maxwell-Garnett equation is valid for particles smaller than the wavelength by at least an order of magnitude and considers the particles as random spherical inclusions in the medium. (1) can be simplified if $|\varepsilon_{\text{eff}} - \varepsilon_h| \ll \varepsilon_h$, or equivalently $\delta \ll 1$, to obtain a closed-form expression for ε_{eff}. This simplification is valid for dispersed multiphase flows of interest for the instrument. Multiple scattering effects are usually neglected in the Maxwell-Garnett equation in dilute particle mixtures ($\delta \ll 1$) due to the very low scattering efficiencies

of particles smaller than the wavelength, as described in Section II-B. Even in high particle concentration mixtures for which multiple scattering could be significant, experiments and simulation have shown that the Maxwell-Garnett equation stays valid [50], [51]

$$\varepsilon_{\text{eff}} = \varepsilon_h \left(1 + 3\delta \frac{\varepsilon_i - \varepsilon_h}{\varepsilon_i + 2\varepsilon_h} \right). \tag{2}$$

The time of flight (TOF) τ of an electromagnetic wave propagating in the fluid-particle mixture between an emitter (TX) and a receiver (RX) is given by (3) as a function of the speed of light in vacuum c_0 and the effective dielectric constant ε_{eff} along the propagation path of the wave $l_{\text{TX,RX}}$

$$\tau = \int_{\text{TX}}^{\text{RX}} \frac{\sqrt{\varepsilon_{\text{eff}}}}{c_0} dl. \tag{3}$$

The time delay $\Delta\tau$ between a wave propagating in a particle-laden medium and a wave propagating in an unladen medium can be measured as a phase shift $\Delta\phi$ by an interferometer. This approach eliminates any offset time due to instrument components (i.e., antennas, transmission lines, etc.)

$$\Delta\phi = 2\pi f_0 \Delta\tau = \frac{2\pi f_0}{c_0} \int_{\text{TX}}^{\text{RX}} \sqrt{\varepsilon_{\text{eff}}} - \sqrt{\varepsilon_h} dl. \tag{4}$$

Combining (2)–(4) provides the phase shift caused by the presence of the particles as a function of the path-integrated particle volume fraction between emitter and receiver, and electromagnetic wave, particle and continuum host medium properties, to obtain the measurement equation for the instrument

$$\Delta\phi = \frac{3\pi f_0}{c_0} \left(\frac{\varepsilon_i - \varepsilon_h}{\varepsilon_i + 2\varepsilon_h} \right) \int_{\text{TX}}^{\text{RX}} \delta dl. \tag{5}$$

Two major benefits of interferometry for measuring the concentration of the dispersed phase are evidenced in (5): the measured phase shift is directly proportional to the path-integrated volume fraction of particles, and it is independent of the particle size distribution (PSD). The proportionality between phase shift and path-integrated volume fraction is advantageous to many realistic applications in which the dispersed particle phase is poorly characterized. The PSD is nonetheless required if the desired output quantity is the number concentration of particles.

B. Extinction Effects

Extinction is a significant challenge for optical diagnostics operating in densely loaded multiphase flows and one of the motivations for the development of the current mm-Wave interferometric instrument. A brief review of extinction theory is useful in explaining how radar interferometry can improve the measurement range of optical methods by several orders of magnitude. An electromagnetic wave propagating through a fluid-particle mixture is scattered and absorbed by the particles, leading to a reduction in flux intensity with distance. This phenomenon is described by the Beer-Lambert law [52] in (6), relating the flux intensity of an electromagnetic wave

I_{RX} measured by a receiver (RX) after propagating through a diffusive material with an initial flux intensity of I_{TX}

$$I_{\text{RX}} = I_{\text{TX}} \exp \left(- \int_{\text{TX}}^{\text{RX}} \mu(l) dl \right) \tag{6}$$

where $\mu(l)$ is the linear attenuation coefficient along the path between (TX) and (RX). In the case of solid particles suspended in a transparent medium, $\mu(l)$ is given by (7) as a function of the particle number distribution $N_p(D)$, number concentration n_p, particle diameters D, and extinction efficiency $Q_{\text{ext}}(D, f_0)$

$$\mu = \frac{1}{4} \pi n_p \int D^2 N_p(D) Q_{\text{ext}}(D, f_0) dD. \tag{7}$$

The extinction efficiency $Q_{\text{ext}}(D, f_0)$ can be analytically derived using Mie theory [53], assuming spherical particles with a known dielectric constant ε or refractive index $\sqrt{\varepsilon}$ as a function of the frequency f_0 (or wavelength λ_0) of the incoming electromagnetic wave and particle diameter D.

When $\lambda_0 \ll D$, scattering is governed by the propagation of light rays inside the particle according to geometric optics. The extinction efficiency in this configuration is constant at $Q_{\text{ext}} = 2$, independent of material properties, frequency, or particle size. This is the situation encountered by most optical diagnostics in particle-laden flows, with particles in the 10–1000 μm range and wavelengths in the 100–1000 nm range. For $\lambda_0 \approx D$, Mie scattering is encountered. The amplitude of the extinction efficiency oscillates with respect to the size parameter, D/λ_0. While this behavior can be used to determine particle sizes and constituent material properties, it is associated with strong extinctions efficiencies and is hard to access for particles in the 10–1000 μm range, as effective wave generation and measurement technologies are not yet available in this section of the electromagnetic spectrum (the "terahertz gap"). When $\lambda_0 \gg D$, Rayleigh scattering happens. The extinction efficiency is proportional to the fourth power of the frequency ($Q_{\text{ext}} \propto f_0^4$), until absorption becomes dominant over scattering ($Q_{\text{ext}} \propto f_0$), depending on the loss tangent of the material. Extinction efficiencies are several orders of magnitude lower in the Rayleigh regime than in the geometric regime.

This means that for particles in the 10–1000 μm range, an instrument operating in the microwave range, $\lambda_0 = 1$–100 mm, will be able to perform measurements at particle concentrations much higher than an optical instrument of comparable power and dynamic range. Fig. 1 shows the extinction efficiency predicted by Mie theory for 105 μm diameter glass particles, very similar to those used in the experiments presented in this article, for different wavelengths and frequencies. The material is assumed to have a dielectric constant $4.5 + j6.75 \times 10^{-2}$ at 77 GHz (3.89 mm) and a refractive index of 1.51 at 650 nm, within the expected range for glass material [54], [55]. The particles have an extinction efficiency 20 000 times lower when illuminated by a 77 GHz mm-Wave radar, than by a visible 650 nm laser.

Equations (5) and (6) can be used to compare the performance of conventional optical diagnostics and mm-Wave interferometry for 105 μm glass particles. Fig. 2 shows the
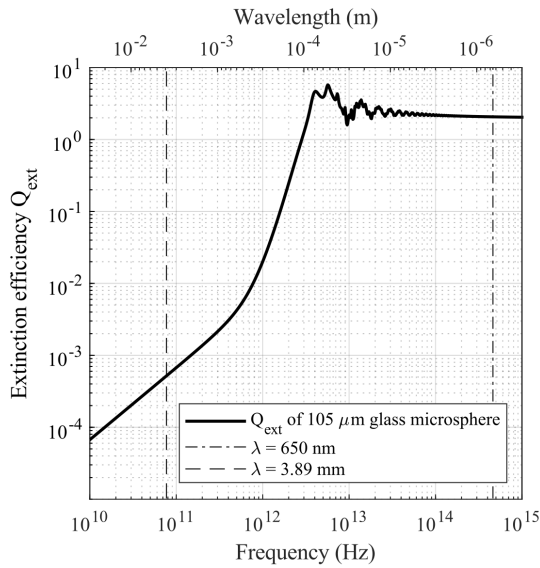
Fig. 1.   Extinction efficiency of 105 μm glass particles as a function of the frequency and wavelength of the electromagnetic wave using Mie theory.
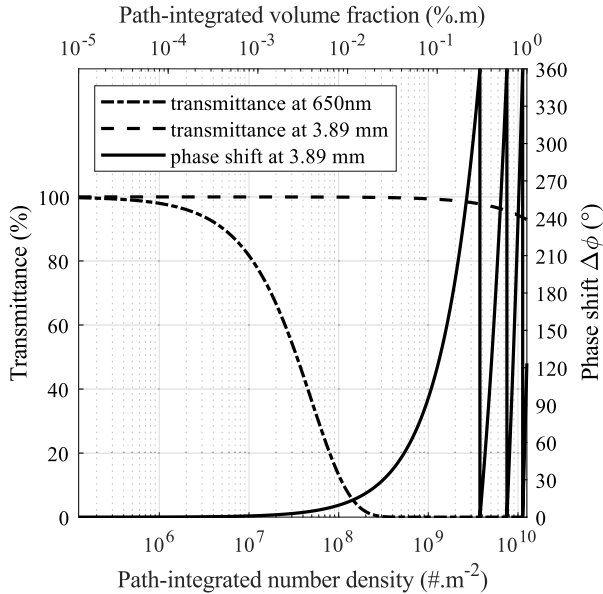

Fig. 2.   Comparison of the attenuation and phase shift of 650 nm laser and 3.89 mm radar (77 GHz) beams traveling through monodisperse glass regolith simulant with a particle diameter of 105 μm.

attenuation of a 650-nm laser beam and the attenuation and phase shift of a 77 GHz mm-Wave radar beam. An important aspect of interferometric measurements is the periodic nature of phase, which can only adopt values contained between [0°, 360°] and must therefore be unwrapped when values exceed this threshold. The maximum phase up to which unwrapping can be reliably performed is an important parameter to determine the measurement range of the interferometer. It depends on the time derivative of the particle volume fraction, on the acquisition frequency, and on the noise of the instrument. If restricted to the unambiguous [0°, 360°] angular range, mm-Wave interferometry is capable of measuring particle concentrations one order of magnitude higher than a laser instrument with a 60 dB dynamic range. The proof-of-concept

interferometer developed in this study has been demonstrated to measure phase up to 20π radians [48]. Such a capability extends its measurement range by another order of magnitude, while the signal attenuation stays at a manageable level.

The ability to measure high particle concentrations is a fundamental advantage of radar interferometry over optical attenuation or scattering-based techniques. Indeed, one could imagine to compensate for excessive extinction by simply increasing the sensitivity of an optical instrument, pushing the dynamic range higher and higher by using more illumination power or a better light sensor. However, this approach is foiled by the exponential nature of light extinction, which results in dramatically diminishing returns in measurement range with increases in sensitivity. For 105 μm particles, increasing the measurement range of an optical attenuation sensor from a path-integrated volume fraction of 2×10^{-2} m–2×10^{-1} m, well within the capability of a mm-Wave interferometer, requires 20 orders of magnitude (200 dB) increase in sensitivity, impossible to achieve. Another benefit of radar interferometry is that it can be tailored to a concentration range of interest: lower frequencies are well-suited for measuring high concentrations, as they are less attenuated and have a higher unambiguous measurement range, while higher frequencies are more sensitive to lower concentrations.

III. EXPERIMENTAL METHODS

A. Instrument

The mm-Wave interferometer used in this work was made of two evaluation boards manufactured by Texas Instruments, the IWR1443BOOST and DCA1000EVM. The IWR1443BOOST carries a IWR1443 radar chip, which integrates a complete 3TX, 4RX 77-81 GHz frequency-modulated continuous wave radar transceiver chip, analog-to-digital converters (ADCs), and a microcontroller in a 10.4×10.4 mm package. The DCA1000EVM is an interfacing board that captures the raw ADC data from the radar and streams it over a 1-GBps Ethernet link to a computer running the mmWaveStudio software. Previous studies by the authors [47] were conducted using the lower frequency IWR6843 as part of a proof-of-concept instrument. It was found to suffer from an excessive imbalance between its in-phase and quadrature channels that leads to high noise. The IWR1443 board does not present this problem. The entire radar system fits in a 130 mm by 130 mm package, weights less 300g (100g for the electronic components themselves) with a peak power consumption of 5 W. The specific radar used emits chirps at a repetition rate of 20 kHz, which defines the temporal resolution of the instrument, similar to conventional high-speed cameras. The chirps have a slope of 100 MHz/μs for a chirp time of 40 μs and idle time between chirps of 10 μs. These parameters correspond to the maximum chirp bandwidth of 4 GHz available to the radar system, which helps minimize clutter and multipath-interference.

Fig. 3 shows the radar interferometer in the subscale experiment that motivated the development of this instrument. The setup reproduces the plume-surface interaction phenomenology of a rocket landing on a planetary surface [39]. A Mach 5 jet impinging on a granular surface leads to a dense cloud
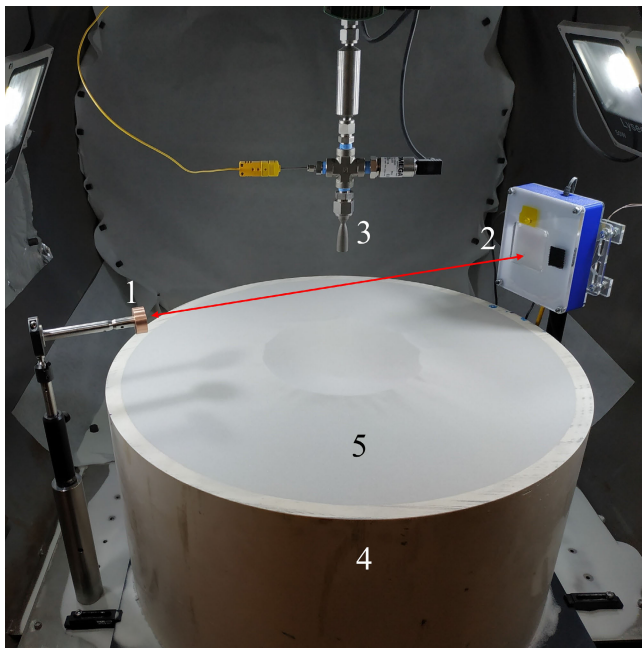
Fig. 3. Instrument in experimental configuration with 1: planar reflector, 2: radar enclosure, 3: thruster, 4: particle bed, and 5: granular surface.

Fig. 4. Concept diagram for the calibration process steps. (a) Optical calibration step. (b) Radar calibration step.

of ejecta and a crater that evolves in time. The radar system setup is identical to that used in this work for demonstrating and calibrating the instrument. A 31.75 mm diameter copper disk reflector defines the line-of-sight with the radar antenna, and thus the measurement chord, which is 58 cm long. The spatial resolution and the measurement volume of the instrument is defined by the apparent angular size of the reflector seen by the radar antenna, 3.1° for the reflector and antenna cross sections and distance between them in this work. A planar reflector is used instead of a more conventional corner cube because its highly directional cross section reduces the effect of multipath-interference. The IWR1443BOOST and DCA1000EVM boards are protected from the particles by a 3-D printed PLA and acrylic enclosure including a PTFE window transparent to mm-Waves. The signal echo corresponding to the reflector is extracted from the radar range data, and the phase of the range bin corresponding to the reflector tracked between each chirp, providing a time-resolved interferometric phase shift measurement.

B. Instrument Calibration

The theoretical framework presented in Section II suggests a linear relationship between the phase shift measured by the instrument and the path-integrated volume particle concentration. The constant of proportionality depends on the radar, host medium, and dispersed phase properties. Provided (5) holds exact, for a given radar it would suffice to know accurately the dielectric constants of the host medium and particles, which could be achieved using a vector network analyzer (VNA) in the mm-Wave range. However, a number of simplifying assumptions are involved in the Maxwell-Garnett theory that although widely used to predict the dielectric constant of mixtures, may render the proportionality factor, or even the linear relation, not accurate. A calibration approach that would
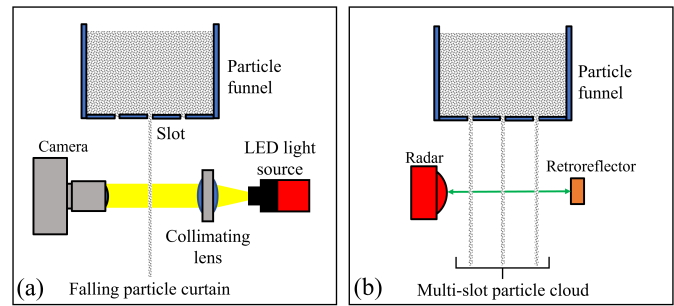
directly serve two purposes was preferred: verifying the linearity between phase shift and path-integrated volume fraction, and directly obtaining the relation between them without the need of measuring dielectric constants, thus avoiding the need for a mm-Wave VNA, an expensive and very specific instrument not widely available. The calibration process is based on the superposition of thin curtains of falling particles, each of which can be individually characterized using an optical counting method. When combined, the curtains provide an optically thick medium with a known path-integrated particle concentration within the measurement range of the instrument. Using this calibration procedure, the instrument measures the travel delay through the same mass of air, laden and unladen, at an interval of a few seconds, which also eliminates any variability due to the host medium. This is in contrast with solid matrix calibration methods [56], which require tight control on the matrix dimensions and physical properties as they directly influence the propagation time of the waves through the mixture. The calibration was implemented using a funnel with individually addressable slots to generate thin curtains of falling particles. The path-integrated concentration of each curtain was measured by a shadowgraphic optical particle-counting method illustrated in Fig. 4(a). Once the particle curtains generated by each slot were characterized, a particle cloud with a known path-integrated concentration was generated by simultaneously opening multiple slots, as shown in Fig. 4(b). By measuring the phase shift for an increasing number of open slots, a calibration curve for phase shift as a function of the number particle concentration is obtained. The calibration set-up covered up to 15% of the unambiguous (0°–360°) measurement range of the instrument. The relationship between these parameters is assumed to remain linear, i.e., the calibration can be extrapolated to higher concentrations.

This methodology requires particle curtains to be identical when individually or jointly operated, which is not the case at ambient conditions due to aerodynamic entertainment. The interaction between the gravity-driven particle flow and the otherwise quiescent surrounding air leads to the generation of a turbulent flow. When multiple particle streams in close proximity are operated, the cross section of a given stream, particle velocities, and thus local particle concentration are modified, leading to a path-averaged concentration that is different from the sum of the contributions of each individual curtain. To avoid these undesired effects the calibration was performed in a chamber in a reduced atmosphere
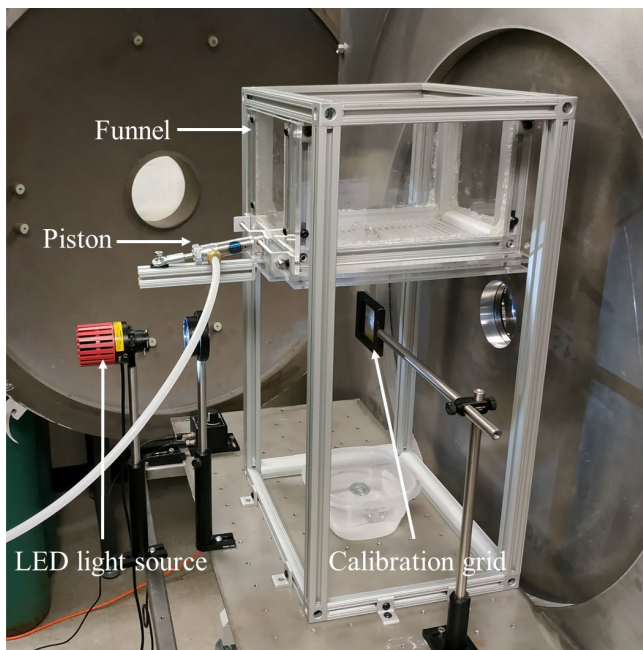
Fig. 5. Piston-actuated slot funnel used for the calibration of the instrument.

Fig. 6. Cross section view of a CT scan of the particle sample. (a) Raw scan. (b) Segmented particles detected in the sample.

at 130 Pa. The repeatability of each slot was evaluated by calculating the mean and 95% prediction interval of the path-integrated concentration over three independent realizations. The custom-made calibration rig as installed in the vacuum chamber is shown in Fig. 5. It consists of a funnel assembly containing a particle hopper, a sliding trapdoor, and an array of 25 individually addressable slots, each with a width of 600 μm, a length of 140 mm, and a spacing of 9.525 mm between the center of each slot. The sliding trapdoor was remotely actuated by a pneumatic piston.

The particles used as regolith simulant were Ballotini solid glass microspheres with a quoted size range of 90–150 μm and a density of 2500 kg.m^{-3}. A 1.5 W white LED collimated by a biconvex lens with a focal length of 100 mm provided the back-illumination for the shadowgraphy particle counting. A 1.3 Mpixel Chronos 1.4 high-speed camera equipped with a Canon EF 100 mm macro lens was used for imaging the particle stream at 1057 frames/s. An exposure of 5 μs was used to prevent motion blur of the falling particles. With an image pixel size of 13.23 μm/pixel, the glass particles were resolved by 53 pixels on average. The following procedure was used to count the particles. First, images were segmented from the background and a sample of well-resolved single particles was selected using a combination of size and roundness thresholds. The total area of all particles in the image was then divided by the average particle area of the selected sample, and a correction factor was applied to account for overlapping. The correction factor was derived by comparing the number of particles counted by the pipeline n_o against synthetic images with a known number of particles n_g. The synthetic images used are representative of real background-subtracted images, with dark circular particles against a white background. Particles are uniformly distributed and their diameter follows the size distribution measured by CT, described in Section III-C. For each value of n_g, ten synthetic images were generated to allow
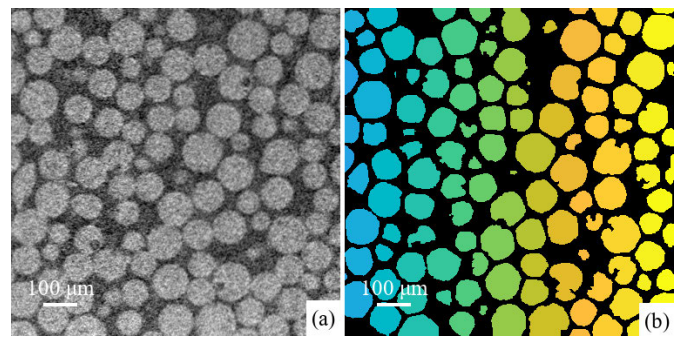
for the derivation of an average count value and prediction interval. A power fit $\hat{n}_g = a(n_o)^b$ provided an estimator $\hat{n}_g$ for the real number of particles n_g as a function of the observed number of particles n_o. The coefficient of determination of the fitting was $r^2 = 0.9994$ with a 95% prediction interval around this fit of $\sigma_{o,95} = \pm 83$ particles.

C. Granular Material Characterization

The phase shift measured by the radar interferometer is proportional to path-integrated volume fraction and is agnostic to the size distribution of the particles. However, because it was calibrated against an optical method providing the path-integrated number concentration of a particle cloud, the conversion of path-integrated number concentration into path-integrated volume fraction requires knowledge of the PSD of the material. While this partially negates one of the advantages of mm-Wave interferometry, it arises from the need of verifying the theoretical measuring principle using robust optical methods for particle-counting in an air-particle mixture environment similar to that of the target experiments. Knowledge of the PSD is not required if the desired output is number concentration of particles and the instrument is calibrated against that quantity, as in the present work. The relation between path-integrated number concentration n_p and path-integrated volume fraction δ is given by the mean of the volume-weighted PSD $\delta = (1/6)\pi n_p (D_{\text{m,v}})^3$.

The size distribution of the particles was measured via X-ray microtomography, in addition to the results from planar shadowgraphy, due to the higher accuracy of CT particle sizing. Uncompacted particles samples were imaged by an Xradia MicroXCT-400 system. The tomographic images, with a voxel size of 2.61 μm/voxel, resolved each particle by 39 000 voxels on average. The images were segmented using a watershed algorithm, resulting in a set of individually-labeled particles whose diameter was measured and binned to determine the sample PSD. The outcome of the segmentation is presented in Fig. 6. For comparison, the particle PSD was also measured by a dry sieve shaker with size breaks at 53, 63, 90, 106, 125, 150, 180, 250, and 350 μm. Results are reported in Section IV-A as volume distributions.

The are two main error contributors to the PSD as derived from micro-CT measurements: error on the particle diameters due to the image resolution, σ_D, and error on the diameter

binning made by the algorithm σ_V. The image resolution error can be estimated as $r_{CT}/\sqrt{2}$, with r_{CT} the voxel size. The binning error σ_V is due to particles that have escaped detection by the watershed segmentation algorithm, usually due to poor convexity. The upper and lower bounds of the volume-weighted mean particle diameter $D_{m,v}$ due to those missing particles were computed as follows. First, the fraction of particles volume missed by the algorithm was estimated by comparing the volume of the raw, unsegmented particles to the volume of segmented particles. Then, two particle volume distributions were generated: $V_l(D)$, in which all the unaccounted volume was assigned to the fifth percentile bin of the distribution, and $V_u(D)$ in which all the unaccounted volume was assigned to the 95th percentile bin. For each distribution, the corresponding mean particle diameter D_{m,V_l} and D_{m,V_u} are computed. While those distributions are highly unlikely, they serve to define upper and lower bounds of the true value of the mean diameter $D_{m,v}$, for which the error can then be defined as

$$\left(\frac{\sigma_{D_{m,v}}}{D_{m,v}}\right)^2 = \left(\frac{D_{m,V_u} - D_{m,V_l}}{2 D_{m,v}}\right)^2 + \left(\frac{r_{CT}}{\sqrt{2} D_{m,v}}\right)^2. \quad (8)$$

The final value of the microCT mean diameter error was 6.7 μm, or 6.1% of $D_{m,v}$. A similar procedure was used to estimate the error on the mean particle diameter obtained by sieving, yielding an error of 9.7 μm, 8.8% of the mean. The mean particle diameter from the planar shadowgraphy images is affected by image resolution and also by the particle identification and postprocessing methods. Shadowgraphy measurements were focused on particle number counting and not optimized for size characterization, and have the largest error on the volume weighted mean diameter. Only the resolution error is provided here as a lowest bound estimate, $r_{pix}/\sqrt{2} = 9.4$ μm, or 7.8% of the mean.

IV. RESULTS

A. Particle Size Measurements

Micro-CT imaging of particle samples provided the particle volume distribution used to convert number to volume concentrations in this work, shown in Fig. 7. Results are compared with those obtained by sieving and direct optical imaging during the calibration. The mean, median, mode, and fifth and 95th percentile diameters are reported in Table I together with the measurement error of each technique. There is a close agreement between the mean diameter as measured via micro-CT and sieving, to within 1%. The median, fifth percentile, and 95th percentiles are also within 5% of each other. The larger gap in the mode diameter of 12% can be explained by the lower resolution of the sieving distribution. The volume distribution obtained through optical imaging appears to be a version of the micro-CT distribution skewed toward higher values by approximately 11 μm. This is considered an artifact due to the thresholding method used in the particle segmentation, affected by the lower resolution of optical imaging.
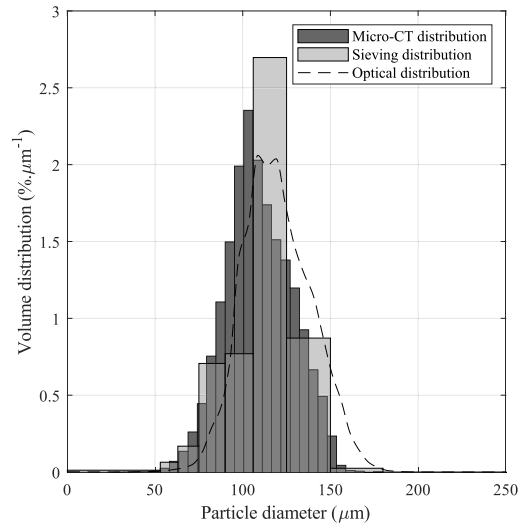

Fig. 7. Comparison between the volume PSD measured by micro-CT scanning, optical imaging, and dry sieving.

TABLE I
VOLUME DISTRIBUTION PROPERTIES OBTAINED THROUGH MICRO-CT
SCANNING, OPTICAL IMAGING, AND SIEVING

Parameter (μm)	Micro-CT	Optical	Sieving
Error	6.7	> 9.4	9.7
Mean	109.2	119.7	110.1
Median	107.8	118.3	113.0
Mode	102.5	108.5	115.5
5th percentile	79.2	90.0	75.8
95th percentile	141.8	153.6	138.1
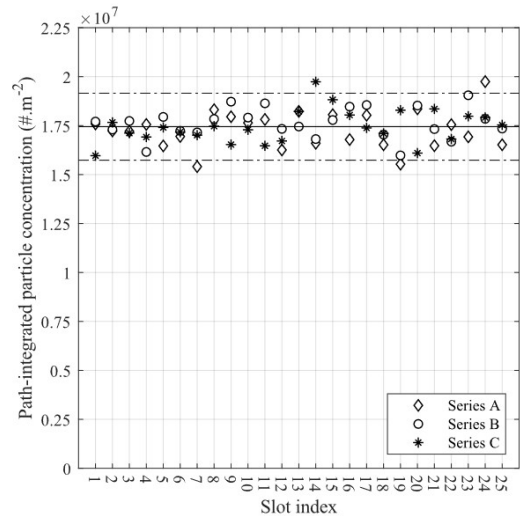
Fig. 8. Path-integrated particle concentration measured by optical counting for each slot, organized in series A–C.

B. Optical Characterization of the Calibration Set-up

Particle concentrations measured for each of the 25 individual funnel slots as described in Section III-B are presented in Fig. 8. Each series, labeled as A–C, corresponds to an independent measurement. Since the spread of the data for each slot is comparable to the total standard deviation of all data points independent of the slot index, each measurement is treated as a single realization of a random variable. The average particle concentration and measurement error for all slots in the

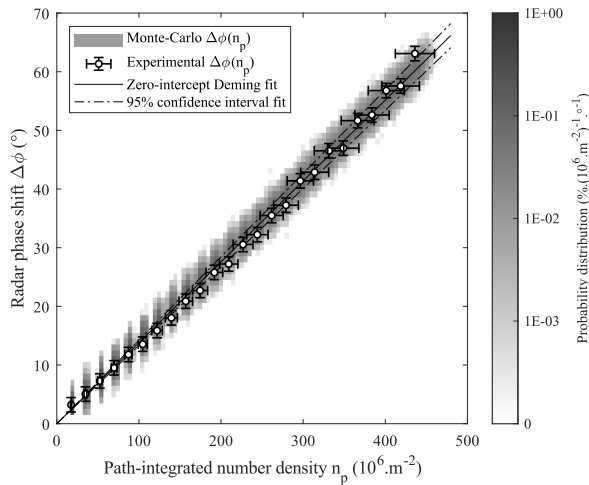Fig. 9. Radar calibration, phase shift versus path-integrated number concentration, with MC probability distribution and associated Deming regression.

2-D images is $n_s = (1.745 \pm 0.043) \times 10^7$ m^{-2}. The standard deviation of the 75 measurement is $\sigma_s = 8.734 \times 10^5$ m^{-2}.

C. Radar Calibration

Radar measurements were conducted for increasing the number of slots open simultaneously. The sequence followed for opening the slots did not have any impact on the calibration regression. Measured phase shift as a function of path-integrated number concentration is shown in Fig. 9. Error bars represent the uncertainty on phase shift and path-integrated number concentration measurements. Due to the presence of error on both parameters, the calibration curve was determined using a zero-intercept Deming regression. MC simulations were used to propagate the combination of systematic and random errors for both phase and integrated number concentration measurements, and to derive a 95% confidence interval fit. The MC probability of a data point being located at a given number density and phase is given by the greyscale contour. The main error source on the radar phase measurement is local clutter, while the optical measurements have error terms related to the output of the slot funnel and to the particle counting algorithm.

The slope of the calibration curve is $\beta_n = (1.379 \pm 0.043) \times 10^{-7}$ m^2. There is an excellent linearity between phase shift and path-integrated particle concentration, with a generalized coefficient of determination $r_g^2 = 0.9964$. This linearity partially verifies the validity of the assumptions involved in the Maxwell-Garnett equation and the theoretical model in (5). The proposed calibration method provides the functional relation between phase shift and path-integrated concentration. Therefore, even if the relation had not been linear, once calibrated the proposed mm-Wave interformeter would still enable path-integrated concentration measurements.

V. DISCUSSION

A. Comparison Between Experimental and Theoretical Results

In this section, the experimental results are compared to the theoretical framework presented in Section II. While the

linearity of the experimental calibration curve is in agreement with the theory, the aim is to compare the measured slope to its theoretical prediction. It should be noted that the theoretical relation is not needed if a calibration such as the one previously described can be performed, which provides the true relation between phase shift and path-integrated particle number density for a given radar and particle-medium mixture. However, verification of the theoretical relation is important for calibration-free methods that would allow knowing the factor of proportionality between path-integrated concentrations and phase shift provided the medium and particle dielectric constants are known with the required measurement accuracy. For this purpose, a statistical model of the calibration experiment based on (5) was used to obtain a probability distribution of possible calibration slope. The uncertainty of our theoretical slope prediction is due to the measured or estimated uncertainties of the parameters involved in the theoretical model. A p-value hypothesis test was conducted between the experimental slope and the theoretical distribution of slopes to quantify their agreement, with a 5% significance level. A sensitivity analysis was conducted to identify the contribution of each parameter to the spread of the model. Finally, the values of the model parameters most in agreement with the experimental slope were derived using maximum likelihood estimation. The theoretical model of the experiment is presented in (9). It combines (5), which predicts the phase shift as a function of path-integrated volume fraction, with the path-integrated volume fraction generated by each particle stream. The use of a passive reflector means that the mm-Waves travel through the particles twice, effectively doubling the signal for a given concentration

$$\Delta\phi = \frac{\pi^2 f_0}{c_0} \frac{\varepsilon_p - \varepsilon_h}{\varepsilon_p + 2\varepsilon_h} D_{m,v}^3 N_s n_s. \tag{9}$$

The parameters involved in the model were modeled as probability distributions according to experimental measurements or a priori estimates from available data in the literature. The radar operating frequency f_0, the number of open slots N_s, and the dielectric constant of the unladen propagation medium (air or vacuum), ε_h, were considered known, not requiring probabilistic modeling. The mean of the volume-weighted particle distribution $D_{m,v}$ and the path-integrated particle number concentration per slot n_s were modeled as Gaussian variables with mean and standard deviation provided by the experimental results described in Sections IV-A and IV-B, respectively. Similarly, a noise term was applied to the radar phase shift $\Delta\phi$ to account for the measurement error reported in Section IV-C. The dielectric constant of the particle material, ε_p, not measured in the current work, was modeled by a uniform probability distribution in the range of 4–7, consistent with values drawn from literature for glass at mm-Wave range [54], [57]. A calibration curve made of 25 data points was generated by varying the number of open slots, N_s. The slope of the calibration curve was calculated using a Deming regression. Given the number of uncertain parameters and the covariance between individual data points due to systematic error terms, MC methods were used for uncertainty propagation with 15 000 repetitions instead of analytical error propagation.
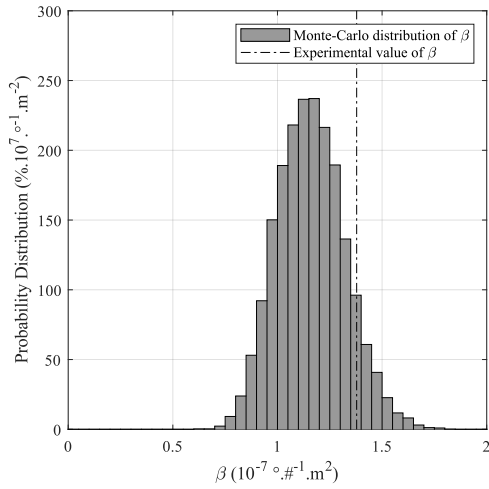
Fig. 10. Probability distribution of calibration points.

TABLE II

95% CONFIDENCE INTERVAL ON β GENERATED BY
ONE-FACTOR-AT-A-TIME SENSITIVITY ANALYSIS FOR EACH
PARAMETER PRESENT IN (9)

Parameter	Confidence interval
$\Delta\phi$	$\pm 8.02\%$
ε_{p}	$\pm 17.9\%$
$D_{\mathrm{m,v}}$	$\pm 25.1\%$
n_{s}	$\pm 13.7\%$

TABLE III

MEAN AND MAXIMUM LIKELIHOOD VALUES OF MODEL PARAMETERS
PROVIDED BY THE MC DISTRIBUTION

Parameter	Mean of MC sample	Maximum likelihood
ε_{p}	5.5	6.93
$D_{\mathrm{m,v}}\,(\mu\mathrm{m})$	109.2	112.2
$n_{\mathrm{s}}\,(10^{-7}\,{}^{\circ}.\#^{-1}.m^2)$	1.745	1.788

The MC probability of a measured phase shift for a given path-integrated number density is represented in greyscale in Fig. 10 along with experimental data for comparison. The mean and 95% confidence interval of the slope distribution predicted by the model are indicated by solid and dashed lines as $1.163 \pm 0.316 \times 10^{-7}$ m^2. The experimental data is in agreement with the numerical model, as it is within the 95% confidence interval, with a two-tailed p-value of 18.6%.

Model uncertainties obscure potential deviations between the experimental data the and theoretical model. A model with high uncertainty on its slope predictions has a correspondingly high risk of false positive. That is, any experimental slope will have a high p-value, even if it does not actually follow the model's base assumption. Efforts to reduce the uncertainty on the slope prediction should be guided by a prior identification of the parameters with a leading impact on the global model uncertainty. For each variable parameter independently ($\Delta\phi$, ε_p, $D_{\mathrm{m,s}}$, n_s), 3000 MC replications were made by randomly choosing values from its probability distribution while keeping all other parameters constant at their mean value. The 95% confidence interval of the calibration slope distributions associated with each parameter is reported in Table II as % of the mean MC slope. The main contributor to the spread of the model is the mean particle diameter of the volume distribution $D_{\mathrm{m,v}}$, followed by ε_p, n_s, and $\Delta\phi$. The leading effect of the mean volume-weighted diameter was expected given that it participates in the functional relation as a cubed parameter. That expectation motivated efforts on accurately measuring the PSD. Using mono-dispersed particles together with higher resolution micro-CT measurements would significantly reduce the uncertainty on model parameters for the purpose of more accurately verifying the theoretical underlying foundation of mm-Wave radar interferometry.

Using the simulated MC data based on the experimental model and parameter distributions, it is possible to find the set of parameters that maximize the likelihood of the model distribution. Those maximum likelihood parameters provide a useful reference for comparison to future parameter measurements. If the theoretical assumptions of the model agree with the calibration measurements, as previously shown within the model uncertainty, the measured value of each parameter converges toward the maximum likelihood value as the accuracy of its measurement increases. The maximum likelihood values for ε_p, $D_{\mathrm{m,v}}$, and n_s were derived by extracting every slope within the experimental margin of error of β_n from the MC dataset. The model parameters realizing those slopes were sorted and binned into probability distributions. The mode of each parameter distribution is the value that maximizes the likelihood of the experimental slope. Maximum likelihood values are reported in Table III along with the mean parameter values in the overall MC distribution for reference. It must be remarked that the maximum likelihood value of each parameter is in the upper range of their distribution. The maximum likelihood dielectric constant, in particular, is close to the edge of the chosen range. These results also suggest that the volume-weighted mean particle diameter could be slightly underestimated by current measurement techniques, possibly due to segmentation thresholds used in the particle sizing and optical particle counting algorithms.

This discussion focused on the role of particle parameter uncertainties in the assessment of theoretical models, or for the inverse determination of particle parameters from the theoretical models combined with experimental data. However, specific knowledge of those parameters or robustness of the theoretical framework is only needed for a calibration-free measurement of concentration from phase shift measurements. If the instrument is calibrated against a gas-particle mixture with a known concentration, using the calibration procedure described or another methodology, the measurement uncertainty is dictated by the calibration. The calibration of the mm-Wave interferometer in this work yielded a path-integrated concentration measurement uncertainty of $\pm 3.12\%$, see Section IV-C.

B. Comparison With Optical Techniques

The ability of the radar interferometer to provide concentration data in particle-laden flows over a wide range of particle loadings is shown in the context of previous works on particle-laden jets. Particle concentration, velocity, and flux are important outputs needed to characterize turbulent mixing

TABLE IV
PARTICLE-LADEN JET EXPERIMENTS REPORTED IN THE LITERATURE. THE NOZZLE DIAMETER, MASS LOADING RATIOS, PARTICLE SIZE, AND BULK DENSITY ARE USED TO ESTIMATE THE PATH-INTEGRATED CONCENTRATION

Source	Jet diameter (mm)	Mass loading ratio	Particle size (μm)	Particle bulk density ($kg.m^{-3}$)	Path-integrated concentration (10^6 #.m^{-2})	Path-integrated volume fraction ($10^{-6}.m$)	Measurement technique
Gillandt *et al.* (2001) [58]	12	1	110	2000	10.2	7.07	LDA
Hardalupas *et al.* (1989) [59]	15	0.86	80	2950	19.2	5.15	PDA
Modarress *et al.* (1984) [60]	20	0.8	200	2990	1.51	6.31	LDA
Shuen *et al.* (1985) [61]	11	0.66	110	2660	4.61	3.22	LDA
Fan *et al.* (1997) [62]	40	0.8	72	1250	154	30.2	LDA
Fleckhaus *et al.* (1987) [63]	13	0.3	132	2590	1.47	1.77	LDA
Gavin *et al.* (1986) [64]	16	0.62	50	3960	45.1	2.95	LDA
Mostafa *et al.* (1989) [65]	25	1	105	2500	19.4	11.8	PDA
Lau *et al.* (2014) [66]	69	0.4	100	1200	51.8	27.1	PN
Longmire *et al.* (1992) [67]	20	0.62	65	2400	42.3	6.09	PN
Fan *et al.* (1990) [68]	42	0.3	70	1250	66.1	11.9	LDM
Aisa *et al.* (2002) [69]	12	0.3	75	2450	10.9	2.40	PDA
Barlow *et al.* (1990) [70]	10	54	165	2500	95.7	225	LDA

and particle dispersion. Experimental studies with particle diameters and bulk densities similar to the present work were selected, with the goal of identifying the capabilities of the mm-Wave within the envelope of concentration conditions relevant and previously explored in particle-laden flows. They are summarized in Table IV. The measurement techniques used include laser Doppler anemometry (LDA), PDA, planar nephelometry (PN), and laser diffraction method (LDM). A challenge present in all optical methods is light extinction, which impedes signal propagation at high particle concentrations. LDA and PDA can provide absolute values of local concentration or flux, but absolute quantities are only accurate in dilute conditions without multiple particles at once within the measurement volume [22], [23]. Therefore, results are most often reported as relative quantities with respect to centerline values or with respect to estimates based on inlet particle mass loading ratios. For the purpose of comparison, the relative concentration results in the reference studies are converted to absolute path-integrated number concentrations. Equation (10) was used to convert the experimental data to path-integrated volume concentrations, where Φ_m is the jet mass loading ratio, ρ_p and ρ_g are the particles bulk and gas densities, respectively, and d is the nozzle exit diameter, considered equal to the jet diameter near the nozzle exit where the particle concentration is highest. This conversion assumes equal average particle and gas velocities, a reasonable estimate for most of the particle Stokes numbers in those works. The mean particle diameter $D_{m,n}$ was used to translate path-integrated volume fractions $\int \delta dl$ to path-integrated number concentrations n_p

$$\int \delta dl = \frac{d}{\frac{\rho_p}{\rho_g \Phi_m} - 1}. \tag{10}$$

Each experimental condition reported is documented in Fig. 11 and corresponds to a path-integrated number concentration and particle size. Data points corresponding to the calibration results presented in this work are included, as well as the range of path-integrated concentrations measured with the mm-Wave interferometer in demonstration experiments for plume-surface interactions [48]. Data points are overlaid on a map of optical absorbance A, (11), calculated using the
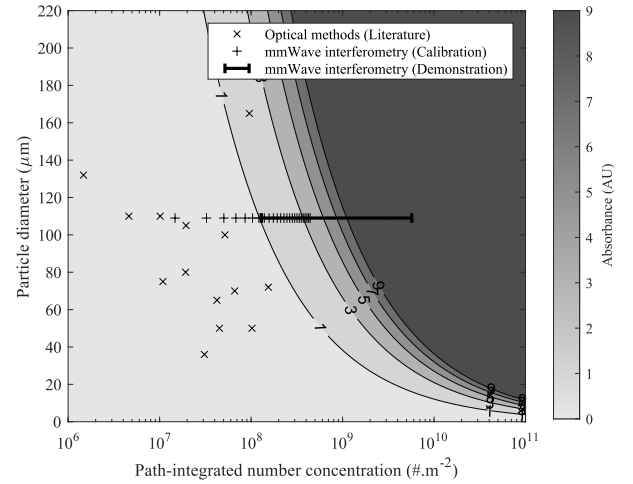

Fig. 11. Contours of optical absorbance as function of path-integrated number concentration and particle diameter. Symbols correspond to published experimental conditions and measurements by mm-Wave interferometer.

Beer-Lambert Law using an extinction efficiency Q_{ext} of 2 for geometric scattering. The optical absorbance associated with each experiment is a measure of the signal extinction that an optical diagnostic encounters for that particle size and path-integrated concentration. Optical techniques are expected to fail once absorbance becomes sufficient to attenuate the signal received by the instrument beyond practical use

$$A = \frac{\pi}{4 ln(10)} Q_{ext} D_{m,n}^2 n_p. \tag{11}$$

Most of the experiments reported in the literature are in the dilute regime, with correspondingly low absorbance values ($A < 1$). Only Barlow and Morrison's work [70] is at a regime where the estimated optical absorbance is above 1 ($A = 1.75$). It is likely that this value is close to the absolute limit for LDA measurements, with authors reporting that higher mass loading ratios were trialed but only a partial signal was recovered by the instrument.

The measurement range of the instrument demonstrated during the calibration significantly overlaps with optical methods at moderate path-integrated concentrations

$(10^7 - 10^8 \text{ m}^{-2})$. The experiments reported by Gillant et al. [58], Shuen et al. [61], Mostafa et al. [65] and Lau and Nathan [66] used particles of similar size to those in the present work ($\pm 10 \ \mu$m), making them useful for one-to-one comparison. Mostafa et al. [65] and Lau and Nathan [66] experiments had similar path-integrated concentrations to those achieved during calibration, while Gillant et al. [58] and Shuen et al.'s citeShuen1984 path-integrated concentrations were lower than the noise floor of the present radar instrument. This indicates that radar interferometry cannot compete with optical methods for very dilute particle-laden flows, the most ideal regime for optical techniques. However, the concentration range during the instrument calibration extends one order of magnitude above those reference experiments, into regions with high optical absorbance. The maximum optical absorbance for the calibration range is 3.6, more than double the absorbance of Barlow and Morrisson's experiment and one to two orders of magnitude higher than the rest of the experiments analyzed. Even higher concentration values were measured using the same instrument during plume-surface interaction demonstration experiments [48], reaching up to $5.71 \times 10^9 \text{ m}^{-2}$. This corresponds to an optical absorbance of 50, far above the capability of any optical system.

Altogether, the new mm-Wave interferometer is able to operate in a wide range of concentrations and particle sizes, complementing optical diagnostics at low to moderate particle loadings, and extending the range of loading conditions measurable experimentally into otherwise inaccessible optically thick flows. The instrument has a number of additional desirable characteristics such as a high sampling rate, low power requirements, and low size, mass, and cost. It provides absolute concentrations of particles, in contrast with most optical techniques other than for very dilute conditions. In addition, for high dielectric constant materials (e.g., titanium dioxide, barium titanate, water, ethanol, as well as most polar liquids), calibration-free measurements are possible, as (7) simplifies into $\Delta\phi \approx (3\pi f_0/c_0) \int_{\text{TX}}^{\text{RX}} \delta dl$, with $\Delta\phi$ independent of the particle dielectric constant. For low dielectric constant material ($\varepsilon < 15$), a calibration procedure is necessary, either following the procedure described in this work, or by measuring the dielectric constant of the material. The spatial resolution of the instrument, of the order of the angular size of the reflector seen by the radar antenna, cannot be compared to that of camera-based optical techniques or point measurements. Higher resolutions are possible at the expense of signal strength (smaller passive reflectors) or complexity (active frequency-coded reflectors).

VI. CONCLUSION

This work presented the development of a mm-Wave radar interferometer capable of measuring absolute values of path-integrated concentrations in optically opaque gas-particle mixtures. The instrument was calibrated against particle number concentration measurements by optical particle-counting, demonstrating a high degree of linearity between measured phase shift and path-integrated concentration. MC simulations were used to evaluate the agreement between the experimental results and theoretical models of wave-particle interactions based on the Maxwell-Garnett theory of effective medium. The experimental results were found to be within the upper margin of error of the theoretical predictions, given in terms of path-integrated volume concentration. While this confirms the validity of the theoretical models, it also indicates a potential bias toward an underestimation of some experimental parameters, the PSD and dielectric constant in particular. Improving the accuracy of those parameters will allow smaller deviations of experimental results from theoretical predictions to be detected, improving theoretical understanding of the technique and paving the way toward simpler calibration procedures based on dielectric constant measurements, or even waiving the need for a calibration entirely in flows involving high dielectric constant material. Nonetheless, if a calibration such as the one proposed in this work is performed, knowledge of the specific particle properties is not required for accurate measurements of path-integrated particle concentrations. The mm-Wave interferometer extends the achievable higher end of the measurement range by at least one order of magnitude with respect to state-of-the-art optical concentration techniques. Enabling absolute measurements of path-integrated concentration, this instrument is particularly relevant for moderate to a high concentration particle-gas mixtures where existing techniques provide at most relative values of local particle densities. Local values can be estimated from path-integrated measurements in mixtures with small concentration gradients. They can also be directly resolved, in time and space, by extending this concept into a tomographic system, currently under development by our group. Other extensions of this work using a mm-Wave radar to measure particle velocities are also envisioned. The instrument can be used in many multiphase flow applications beyond the specific plume-surface interaction problem that motivated its development. Glass particles in the 80–140 μm range were used in this work, but the same principles apply to other particle size and material, such as liquid droplets or soil particles. With a low weight, low cost, compact design, and high frequency resolution (above 20 kHz for the specific radar presented), it is well suited for laboratory and field applications where more expensive, fragile, and bulkier optical equipment is not practical.

REFERENCES

[1] S. Balachandar and J. K. Eaton, "Turbulent dispersed multiphase flow," *Annu. Rev. Fluid Mech.*, vol. 42, no. 1, pp. 111–133, Jan. 2010.

[2] J. Werther, "Measurement techniques in fluidized beds," *Powder Technol.*, vol. 102, no. 1, pp. 15–36, Apr. 1999.

[3] A. M. Squires, M. Kwauk, and A. A. Avidan, "Fluid beds: At last, challenging two entrenched practices," *Science*, vol. 230, no. 4732, pp. 1329–1337, Dec. 1985.

[4] Z. Dong, X. Liu, H. Wang, and X. Wang, "Aeolian sand transport: A wind tunnel model," *Sedimentary Geol.*, vol. 161, nos. 1–2, pp. 71–83, Sep. 2003.

[5] M. I. Cantero, S. Balachandar, and M. H. García, "An Eulerian–Eulerian model for gravity currents driven by inertial particles," *Int. J. Multiphase Flow*, vol. 34, no. 5, pp. 484–501, May 2008.

[6] A. S. Blair, "Dust explosion incidents and regulations in the United States," *J. Loss Prevention Process Industries*, vol. 20, nos. 4–6, pp. 523–529, Jul. 2007.

[7] H. Dregne, "Desertification of arid lands," in *Physics of Desertification*. Dordrecht, The Netherlands: Springer, Apr. 1986, pp. 4–34.

[8] R. Whittle. (Jul. 2019). *Army Seeks Industry Help to Stop Brownout Deaths $1B in Losses*. [Online]. Available: https://breakingdefense.com/2015/10/army-seeks-industry-help-to-stop-brownout-deaths-1b-in-losses/

[9] D. Batcheldor and J. Mantovani, "Mapping lunar lander plume ejecta trajectories to lunar surface elevations," *Earth Space*, pp. 17–26, Jan. 2023.

[10] J. G. Mantovani, B. T. Vu, and J. E. Lane, "Modeling of lunar dust particle trajectories for rocket plume-surface impingement studies," *Earth Space*, pp. 127–135, Apr. 2021.

[11] P. T. Metzger, C. D. Immer, C. M. Donahue, B. T. Vu, R. C. Latta, and M. Deyo-Svendsen, "Jet-induced cratering of a granular surface with application to lunar spaceports," *J. Aerosp. Eng.*, vol. 22, no. 1, pp. 24–32, Jan. 2009.

[12] J. M. Weisberger, P. M. Danehy, T. W. Fahringer, B. F. Bathel, and O. Tyrrell, "Development of a terrain mapping/crater evolution measurement using diffractive optical elements," in *Proc. AIAA AVIATION Forum*, Jun. 2022, p. 3562.

[13] M. Mehta et al., "Explosive erosion during the Phoenix landing exposes subsurface water on Mars," *Icarus*, vol. 211, no. 1, pp. 172–194, Jan. 2011.

[14] C. Immer, J. Lane, P. Metzger, and S. Clements, "Apollo video photogrammetry estimation of plume impingement effects," *Icarus*, vol. 214, no. 1, pp. 46–52, Jul. 2011.

[15] M. A. van der Hoef, M. van Sint Annaland, N. G. Deen, and J. A. M. Kuipers, "Numerical simulation of dense gas-solid fluidized beds: A multiscale modeling strategy," *Annu. Rev. Fluid Mech.*, vol. 40, no. 1, pp. 47–70, Jan. 2008.

[16] M. Esmaily, L. Villafane, A. J. Banko, G. Iaccarino, J. K. Eaton, and A. Mani, "A benchmark for particle-laden turbulent duct flow: A joint computational and experimental study," *Int. J. Multiphase Flow*, vol. 132, Nov. 2020, Art. no. 103410.

[17] M. Di Renzo, P. L. Johnson, M. Bassenne, L. Villafañe, and J. Urzay, "Mitigation of turbophoresis in particle-laden turbulent channel flows by using incident electric fields," *Phys. Rev. Fluids*, vol. 4, no. 12, Dec. 2019, Art. no. 124303.

[18] W. Ge et al., "Discrete simulation of granular and particle-fluid flows: From fundamental study to engineering application," *Rev. Chem. Eng.*, vol. 33, no. 6, pp. 551–623, Nov. 2017.

[19] J. West and P. Liever, "Gas-particle interaction model development in plume surface interaction erosion and cratering," in *Proc. AIAA SCITECH Forum*, Jan. 2022, p. 2321.

[20] J. Capecelatro, "Modeling high-speed gas–particle flows relevant to spacecraft landings," *Int. J. Multiphase Flow*, vol. 150, May 2022, Art. no. 104008.

[21] P. A. Liever and J. West, "Particle interaction physics model formulation for plume-surface interaction erosion and cratering," in *Proc. AIAA SCITECH Forum*, Jan. 2022, p. 2317.

[22] M. Sommerfeld and H.-H. Qiu, "Particle concentration measurements by phase-Doppler anemometry in complex dispersed two-phase flows," *Exp. Fluids*, vol. 18, no. 3, pp. 187–198, Jan. 1995.

[23] J. D. Kulick, J. R. Fessler, and J. K. Eaton, "Particle response and turbulence modification in fully developed channel flow," *J. Fluid Mech.*, vol. 277, pp. 109–134, Oct. 1994.

[24] A. Aliseda, A. Cartellier, F. Hainaux, and J. C. Lasheras, "Effect of preferential concentration on the settling velocity of heavy particles in homogeneous isotropic turbulence," *J. Fluid Mech.*, vol. 468, pp. 77–105, Oct. 2002.

[25] C. Poelma, "Measurement in opaque flows: A review of measurement techniques for dispersed multiphase flows," *Acta Mechanica*, vol. 231, no. 6, pp. 2089–2111, Jun. 2020.

[26] A. M. Korzun et al., "Design of a subscale, inert gas test for plume-surface interactions in a reduced pressure environment," in *Proc. AIAA SCITECH Forum*, Jan. 2022, p. 1808.

[27] H. Grosshans, L. Villafañe, A. Banko, and M. V. Papalexandris, "Case study on the influence of electrostatic charges on particle concentration in turbulent duct flows," *Powder Technol.*, vol. 357, pp. 46–53, Dec. 2019.

[28] A. Aliseda and T. J. Heindel, "X-ray flow visualization in multiphase flows," *Annu. Rev. Fluid Mech.*, vol. 53, no. 1, pp. 543–567, Jan. 2021.

[29] J. A. Grant, M. J. Morgan, J. R. Davis, D. R. Davies, and P. Wells, "X-ray diffraction microtomography," *Meas. Sci. Technol.*, vol. 4, no. 1, pp. 83–87, Jan. 1993.

[30] S. Kumar and M. Dudukovic, "Computer assisted gamma and X-ray tomography: Applications to multiphase flow systems," in *Non-Invasive Monitoring of Multiphase Flows*. Amsterdam, The Netherlands: Elsevier, Jan. 1997, pp. 47–103.

[31] J. T. Lindsay, J. D. Jones, and C. W. Kauffman, "Real time neutron radiography and its' application to the study of internal combustion engines and fluid flow," in *Neutron Radiography*, J. P. Barton, G. Farny, J.-L. Person, and H. Röttger, Eds. Dordrecht, The Netherlands: Springer, Jun. 1986, pp. 579–586.

[32] D. Benton and D. Parker, "Non-medical applications of positron emission tomography," in *Non-Invasive Monitoring of Multiphase Flows*. Amsterdam, The Netherlands: Elsevier, Jan. 1997, pp. 161–184.

[33] S. Ramaswamy, M. McCarthy, and R. Powell, "Pulp flow visualization using NMR imaging," in *Non-Invasive Monitoring of Multiphase Flows*, J. Chaouki, F. Larachi, and M. P. Dudukovic, Eds. Amsterdam, The Netherlands: Elsevier, Jan. 1997, pp. 247–262.

[34] C. Liu, C. Xue, B. Zhang, G. Zhang, and C. He, "The application of an ultrasound tomography algorithm in a novel ring 3D ultrasound imaging system," *Sensors*, vol. 18, no. 5, p. 1332, Apr. 2018.

[35] Z. Wu and H. Wang, "Microwave tomography for industrial process imaging: Example applications and experimental results," *IEEE Antennas Propag. Mag.*, vol. 59, no. 5, pp. 61–71, Oct. 2017.

[36] H. Wang and W. Yang, "Application of electrical capacitance tomography in circulating fluidised beds—A review," *Appl. Thermal Eng.*, vol. 176, Jul. 2020, Art. no. 115311.

[37] M. A. Sattar, M. M. Garcia, R. Banasiak, L. M. Portela, and L. Babout, "Electrical resistance tomography for control applications: Quantitative study of the gas-liquid distribution inside a cyclone," *Sensors*, vol. 20, no. 21, p. 6069, Oct. 2020.

[38] L. M. Heikkinen, J. Kourunen, T. Savolainen, P. J. Vauhkonen, J. P. Kaipio, and M. Vauhkonen, "Real time three-dimensional electrical impedance tomography applied in multiphase flow imaging," *Meas. Sci. Technol.*, vol. 17, no. 8, pp. 2083–2087, Jul. 2006.

[39] H. Al-Rashdan, "Supersonic underexpanded flow visualization in sub-atmospheric facility," in *Proc. AIAA Aviation Forum*, Jun. 2021, p. 2859.

[40] K. Mostov, E. Liptsen, and R. Boutchko, "Medical applications of shortwave FM radar: Remote monitoring of cardiac and respiratory motion," *Med. Phys.*, vol. 37, no. 3, pp. 1332–1338, Mar. 2010.

[41] G. Wang, J.-M. Munoz-Ferreras, C. Gu, C. Li, and R. Gomez-Garcia, "Application of linear-frequency-modulated continuous-wave (LFMCW) radars for tracking of vital signs," *IEEE Trans. Microw. Theory Techn.*, vol. 62, no. 6, pp. 1387–1399, Jun. 2014.

[42] A. Och et al., "High-resolution millimeter-wave tomography system for nondestructive testing of low-permittivity materials," *IEEE Trans. Microw. Theory Techn.*, vol. 69, no. 1, pp. 1105–1113, Jan. 2021.

[43] M. Pauli et al., "Miniaturized millimeter-wave radar sensor for high-accuracy applications," *IEEE Trans. Microw. Theory Techn.*, vol. 65, no. 5, pp. 1707–1715, May 2017.

[44] O. Tudisco et al., "A microwave interferometer for small and tenuous plasma density measurements," *Rev. Sci. Instrum.*, vol. 84, no. 3, Mar. 2013, Art. no. 033505.

[45] K. Akhtar, J. E. Scharer, S. M. Tysk, and E. Kho, "Plasma interferometry at high pressures," *Rev. Sci. Instrum.*, vol. 74, no. 2, pp. 996–1001, Feb. 2003.

[46] L. Porte, C. L. Rettig, W. A. Peebles, and X. Ngyuen, "Design and operation of a low cost, reliable millimeter-wave interferometer," *Rev. Sci. Instrum.*, vol. 70, no. 1, pp. 1082–1084, Jan. 1999.

[47] N. Rasmont, H. T. Al-Rashdan, G. Elliott, J. Rovey, and L. Villafañe Roca, "Millimeter wave interferometry for ejecta concentration measurements in plume-surface interactions," in *Proc. AIAA SCITECH Forum*, Jan. 2022, p. 2421.

[48] N. Rasmont, H. T. Al-Rashdan, G. Elliott, J. Rovey, and L. V. Roca, "Spatially distributed measurements of ejecta concentrations in plume-surface interactions using millimeter wave interferometry," in *Proc. AIAA Scitech Forum*, Jan. 2023, p. 465. [Online]. Available: https://arc.aiaa.org/doi/abs/10.2514/6.2021-2859

[49] V. A. Markel, "Introduction to the Maxwell Garnett approximation: Tutorial," *J. Opt. Soc. Amer. A, Opt. Image Sci.*, vol. 33, no. 7, pp. 1244–1256, Jul. 2016.

[50] P. Mallet, C. A. Guérin, and A. Sentenac, "Maxwell-garnett mixing rule in the presence of multiple scattering: Derivation and accuracy," *Phys. Rev. B, Condens. Matter*, vol. 72, no. 1, Jul. 2005, Art. no. 014205, doi: 10.1103/PhysRevB.72.014205.

[51] A. H. Sihvola and J. A. Kong, "Effective permittivity of dielectric mixtures," *IEEE Trans. Geosci. Remote Sens.*, vol. 26, no. 4, pp. 420–429, Jul. 1988, doi: 10.1109/36.3045.

[52] A. J. Banko, L. Villafañe, J. H. Kim, M. Esmaily, and J. K. Eaton, "Stochastic modeling of direct radiation transmission in particle-laden turbulent flow," *J. Quant. Spectrosc. Radiat. Transf.*, vol. 226, pp. 1–18, Mar. 2019.

[53] D. L. Mitchell, "Parameterization of the mie extinction and absorption coefficients for water clouds," *J. Atmos. Sci.*, vol. 57, no. 9, pp. 1311–1326, May 2000.

[54] SCHOTT AG. (2019). *Electrical Properties of SCHOTT Thin Glasses*. [Online]. Available: https://www.schott.com/d/corporate/6a54c237-f03d-4699-987e-3edd56dd66a7/row-schott-electrical-properties-datenflyer-view-2019-05-24.pdf

[55] SCHOTT AG. *Datasheets and Downloads for SCHOTT Optical Glass*. Accessed: Feb. 10, 2023. [Online]. Available: https://www.schott.com/en-nl/products/optical-glass-p1000267/downloads

[56] R. Tempke, C. Wildfire, D. Shekhawat, and T. Musho, "Dielectric measurement of powdery materials using a coaxial transmission line," *IET Sci., Meas. Technol.*, vol. 14, no. 10, pp. 972–978, Dec. 2020.

[57] J. W. Lamb, "Miscellaneous data on materials for millimetre and submillimetre optics," *Int. J. Infr. Millim. Waves*, vol. 17, no. 12, pp. 1997–2034, Dec. 1996.

[58] I. Gillandt, U. Fritsching, and K. Bauckhage, "Measurement of phase interaction in dispersed gas/particle two-phase flow," *Int. J. Multiphase Flow*, vol. 27, no. 8, pp. 1313–1332, Aug. 2001.

[59] Y. Hardalupas, A. M. K. P. Taylor, and J. H. Whitelaw, "Velocity and particle-flux characteristics of trubulent particle-laden jets," *Proc. R. Soc. A, Math. Phys. Eng. Sci.*, vol. 426, no. 1870, pp. 31–78, Nov. 1989.

[60] D. Modarress, H. Tan, and S. Elghobashi, "Two-component LDA measurement in a two-phase turbulent jet," *AIAA J.*, vol. 22, no. 5, pp. 624–630, May 1984.

[61] J.-S. Shuen, A. S. P. Solomon, Q.-F. Zhang, and G. M. Faeth, "Structure of particle-laden jets–measurements and predictions," *AIAA J.*, vol. 23, no. 3, pp. 396–404, Mar. 1985.

[62] J. Fan, X. Zhang, L. Chen, and K. Cen, "New stochastic particle dispersion modeling of a turbulent particle-laden round jet," *Chem. Eng. J.*, vol. 66, no. 3, pp. 207–215, Mar. 1997.

[63] D. Fleckhaus, K. Hishida, and M. Maeda, "Effect of laden solid particles on the turbulent flow structure of a round free jet," *Exp. Fluids*, vol. 5, no. 5, pp. 323–333, 1987.

[64] L. B. Gavin, A. S. Mul'gi, and V. V. Shor, "Numerical and experimental study of a nonisothermal turbulent jet with a heavy impurity," *J. Eng. Phys.*, vol. 50, no. 5, pp. 505–511, May 1986.

[65] A. A. Mostafa, H. C. Mongia, V. G. McDonell, and G. S. Samuelsen, "Evolution of particle-laden jet flows—A theoretical and experimental study," *AIAA J.*, vol. 27, no. 2, pp. 167–183, Feb. 1989.

[66] T. C. W. Lau and G. J. Nathan, "Influence of Stokes number on the velocity and concentration distributions in particle-laden jets," *J. Fluid Mech.*, vol. 757, pp. 432–457, Oct. 2014.

[67] E. K. Longmire and J. K. Eaton, "Structure of a particle-laden round jet," *J. Fluid Mech.*, vol. 236, pp. 217–257, Mar. 1992.

[68] J. Fan, L. Zhang, H. Zhao, and K. Cen, "Particle concentration and particle size measurements in a particle laden turbulent free jet," *Exp. Fluids*, vol. 9, no. 6, pp. 320–322, Sep. 1990.

[69] L. Aisa, J. Garcia, L. Cerecedo, I. Garcia Palacin, and E. Calvo, "Particle concentration and local mass flux measurements in two-phase flows with PDA. Application to a study on the dispersion of spherical particles in a turbulent air jet," *Int. J. Multiphase Flow*, vol. 28, no. 2, pp. 301–324, Feb. 2002.

[70] R. S. Barlow and C. Q. Morrison, "Two-phase velocity measurements in dense particle-laden jets," *Exp. Fluids*, vol. 9, nos. 1–2, pp. 93–104, 1990.

Nicolas Rasmont (Graduate Student Member, IEEE) received the B.Sc. degree in aerospace engineering from the French National Institute for Aeronautics and Space (ISAE-SUPAERO), Toulouse, France, in 2018, and the double M.Sc. degree in aerospace engineering from the University of Illinois at Urbana-Champaign (UIUC), Urbana, IL, USA, and ISAE-SUPAERO, in 2020. He is currently pursuing the Ph.D. degree at the Department of Aerospace Engineering, UIUC.

Mr. Rasmont received the NASA Future Investigator in NASA Earth and Space Science and Technology (FINESST) Fellowship for his work on plume-surface diagnostics.

Hussein Al-Rashdan received the B.Sc. degree in aerospace engineering from the University of Illinois at Urbana-Champaign (UIUC), Urbana, IL, USA, in 2018, where he is currently pursuing the Ph.D. degree at the Department of Aerospace Engineering.

Mr. Al-Rashdan has received the Department of Education Graduate Assistance in Areas of National Need (DOE GAANN) Fellowship for his work on plume surface interaction non-intrusive optical diagnostics.

Gregory Elliott received the Ph.D. degree in mechanical engineering from The Ohio State University, Columbus, OH, USA, in 1993.

He is currently a Professor with the Aerospace Engineering Department, University of Illinois at Urbana-Champaign, Urbana, IL, USA. His research covers areas of experimental fluid mechanics, high-speed flows, plasmas, combustion, and laser diagnostics.

Prof. Elliott is a Fellow of American Society of Mechanical Engineers (ASME), an Associate Fellow of American Institute of Aeronautics and Astronautics (AIAA), and was a recipient of the NASA Group Achievement Award in 2011.

Joshua Rovey received the Ph.D. degree in aerospace engineering from the University of Michigan, Ann Arbor, MI, USA, in 2006.

He is currently a Professor of aerospace engineering at the University of Illinois Urbana-Champaign, Urbana, IL, USA, where he leads the Space Propulsion Laboratory. He has authored over 150 conference and journal publications in chemical and electric space propulsion, propellant development, and plasma studies.

Prof. Rovey is an American Institute of Aeronautics and Astronautics (AIAA) Associate Fellow.

Laura Villafañe received the Ph.D. degree from the Von Karman Institute for Fluid Dynamics, Sint-Genesius-Rode, Belgium, in 2014.

She is currently an Assistant Professor of aerospace engineering at the University of Illinois at Urbana-Champaign, Urbana, IL, USA. Prior to joining UIUC, she was a Post-Doctoral Fellow and a Research Engineer at Stanford University, Stanford, CA, USA. Her research focuses on multiphase, unsteady, and separated flows, and non-intrusive flow diagnostics.

Prof. Villafañe is an American Physical Society (APS) and American Institute of Aeronautics and Astronautics (AIAA) Senior Member.